

Engineering Na⁺-layer spacings to stabilize Mn-based layered cathodes for sodium-ion batteries

Wenhua Zuo¹, Xiangsi Liu¹, Jimin Qiu², Dexin Zhang³, Zhumei Xiao¹, Jisheng Xie¹, Fucheng Ren⁴, Jinming Wang⁵, Yixiao Li¹, Gregorio F. Ortiz ⁶, Wen Wen⁷, Shunqing Wu ³, Ming-Sheng Wang ⁵✉, Riqiang Fu ⁸ & Yong Yang ^{1,4}✉

Layered transition metal oxides are the most important cathode materials for Li/Na/K ion batteries. Suppressing undesirable phase transformations during charge-discharge processes is a critical and fundamental challenge towards the rational design of high-performance layered oxide cathodes. Here we report a shale-like Na_xMnO₂ (S-NMO) electrode that is derived from a simple but effective water-mediated strategy. This strategy expands the Na⁺ layer spacings of P2-type Na_{0.67}MnO₂ and transforms the particles into accordion-like morphology. Therefore, the S-NMO electrode exhibits improved Na⁺ mobility and near-zero-strain property during charge-discharge processes, which leads to outstanding rate capability (100 mAh g⁻¹ at the operation time of 6 min) and cycling stability (>3000 cycles). In addition, the water-mediated strategy is feasible to other layered sodium oxides and the obtained S-NMO electrode has an excellent tolerance to humidity. This work demonstrates that engineering the spacings of alkali-metal layer is an effective strategy to stabilize the structure of layered transition metal oxides.

¹State Key Laboratory for Physical Chemistry of Solid Surfaces, Department of Chemistry, College of Chemistry and Chemical Engineering, Xiamen University, Xiamen, People's Republic of China. ²School of Advanced Materials, Peking University Shenzhen Graduate School, Shenzhen, People's Republic of China. ³Department of Physics, Collaborative Innovation Center for Optoelectronic Semiconductors and Efficient Devices, Key Laboratory of Low Dimensional Condensed Matter Physics, Xiamen University, Xiamen, People's Republic of China. ⁴School of Energy Research, Xiamen University, Xiamen, People's Republic of China. ⁵State Key Laboratory for Physical Chemistry of Solid Surfaces, College of Materials, Xiamen University, Xiamen, Fujian, People's Republic of China. ⁶Department of Inorganic Chemistry and Chemical Engineering, University Research Institute in Nanochemistry (IUNAN), University of Córdoba, Córdoba, Spain. ⁷Shanghai Advanced Research Institute, Shanghai Synchrotron Radiation Facility, Chinese Academy of Sciences, Shanghai, People's Republic of China. ⁸National High Magnetic Field Laboratory, Tallahassee, FL, USA. ✉email: mshwang@xmu.edu.cn; yyang@xmu.edu.cn

Lithium-ion batteries (LIBs) dominate the markets for portable electronics and electric vehicles^{1,2}. As complementary candidates to LIBs, sodium-ion batteries (NIBs) hold the promise for large-scale energy storage, such as national and smart grids^{3–6}. Composed of the ordered stacking of alkali-metal (Li⁺/Na⁺) layers and transition metal (TmO₂) layers, the layered transition metal oxides (LiTmO₂ and Na_xTmO₂) are prevailing cathodes for both LIBs and NIBs owing to their scalable synthesis, great variety in compositions, superior theoretical specific capacity, and reliable electrochemical performances^{7–10}. However, the charge–discharge processes of LiTmO₂ and Na_xTmO₂ cathodes are typically accompanied by undesirable phase transformations and the subsequent unsatisfied specific capacity and cycling stability. The major causes for such phase transformations include the migration of Tm ions that results in layer-to-spinel transformation, the anisotropic change of Tm–O bonds during the redox reactions of Tm/O ions, and the evolutions of electrostatic interactions between O–O, Na(Li)–O, and Tm–O.

Since utilized as the positive electrodes in alkaline Zn/MnO₂ batteries in the early 1900s¹¹, the Mn-based oxides have attracted enormous attention as battery materials due to the advantages of high abundance in the earth's crust (11.3-folds of Ni and 38.1-folds of Co), large annual production, and low cost of Mn sources. The present LiTmO₂ cathodes, however, rely heavily on scarce, expensive, and thermally unstable Co and Ni elements, because the Mn-redox active LiTmO₂ suffers from the interlayer migration of Mn ions during repeated Li⁺ (de-)intercalation and rapid capacity decay^{12,13}. However, the Mn-based Na_xTmO₂, such as P2-Na_{0.67}MnO₂¹³ and P2-Na-Fe-Mn-O¹⁴ series, exhibited high specific capacity and better redox reversibility, which highly meet the requirements for sustainable and cost-effective NIBs.

To address the challenge of phase transformations in Mn-based Na_xTmO₂, various design and modification strategies have been developed. Substituting Jahn–Teller center (Mn³⁺) with inert elements, such as Li⁺^{15,16}, Mg²⁺^{17–19}, Zn²⁺^{20,21}, and Al³⁺^{22,23}, is reported to improve the structural and cycling stability, but usually compromises the specific capacity and energy density. Another effective strategy is to regulate the pristine structure of layered oxides. For example, Tm vacancies, whose concentration can be regulated by adopting different cooling processes, have been reported to influence the reversible capacity and structural changes of Na_xTmO₂ greatly^{13,24,25}. However, the application of the Mn-based Na_xTmO₂ is still thwarted by unsatisfied electrochemical performances. Therefore, developing new designing strategies to tackle these issues are necessary and urgent.

Electrostatic interaction is a decisive factor for understanding the phase transformations of layered oxides. For pristine structure, the localized electron distributions in layered transition metal oxides determine the stacking modes (P- or O-type stacking) of layered sodium oxides^{26,27}. During charge and discharge processes, the adjacent TmO₂ layers glide at the highly charged states to balance the O–O repulsion and Li(Na)–O attraction, such as the O3–H1–3 transition in LiCoO₂^{28–30}, collapse of *c* parameter in LiNi_xCo_yMn_{z-x-y}O₂^{31–33}, P2–O2 transition in P2-Na_{0.67}Ni_{0.33}Mn_{0.67}O₂¹⁰, and P2–OP4 transformation in P2-Na_{0.67}Zn_{0.2}Mn_{0.8}O₂²⁰. Besides Tm types and the Li⁺/Na⁺ contents, the electrostatic interactions of layered oxides (Fig. 1), including O–O repulsion, O–Na(Li) attraction, and van der Waals (vdW) force, are greatly influenced by the Li⁺/Na⁺ layer spacings (*d*_{O–O}). Taking P2-Na_{0.67}MnO₂ as an example (Supplementary Fig. 1), as Na⁺ layer spacings increase from 3.8 to 6.0 Å, the electrostatic repulsion of O1–O2 atoms (297 eV) and electrostatic attraction of Na1–O2 atoms (–157 eV) decay by 18% (54 eV) and 12% (–18 eV), respectively. Simultaneously, the vdW interaction also decreases gradually with the increment of Na⁺ layer spacings (Supplementary Fig. 2), although the strength of vdW interaction

(0–3.5 eV) is much weaker than that of the O–O and Na–O bonds. Therefore, by increasing the alkali-metal (Li⁺/Na⁺) layer spacings, the coulombic interactions in layered oxides decrease considerably, which provides a possibility to facilitate their Li⁺/Na⁺ mobility, suppress their phase transformations, and improve their electrochemical performances.

This work uses P2-Na_{0.67}MnO₂ as a model material to study the influence of the changes of Na⁺ layer spacings on the electrochemical properties of layered oxides. We propose a non-hazardous water-mediated strategy to increase the Na⁺ layer spacings in P2-Na_{0.67}MnO₂. The obtained sample exhibits a shale-like structure (S-NMO), accordion-like morphology, and exceptional electrochemical performances. Without any further electrode/electrolyte modifications, the S-NMO delivers a high specific capacity of 181 mAh g^{–1} with no obvious capacity fade after 100 cycles at 0.1 C, outstanding rate performance, and long cycling stability of 3000 cycles with 83% capacity retention. In situ synchrotron X-ray diffraction (XRD) and ex situ magic-angle-spinning nuclear magnetic resonance spectroscopy (MAS NMR) results reveal that the S-NMO electrode exhibits a zero-strain property along the *c* axis with only 1.96% volume change during charge–discharge processes. This water-mediated engineering strategy is applicable for other Mn- and Fe-based layered oxides, such as Na_{0.67}Zn_{0.1}Mn_{0.9}O₂ and Na_{0.67}Fe_{0.1}Mn_{0.9}O₂. In addition, the obtained S-NMO cathodes can be stored in moist atmospheres and thus lowering the manufacture and storage cost of Mn-based layered oxides.

Results

Materials synthesis and characterizations. A schematic illustration of the facile water-mediated process is shown in Fig. 2, along with the structural diagrams and morphologies of Na_xMnO₂ materials at different stages. Synthesized Na_{0.67}MnO₂ particles have an irregular shape and smooth surface. XRD patterns in Fig. 3a reveal that the pristine Na_{0.67}MnO₂ has a P2-type structure with *P6₃/mmc* space group (JCPDF no. 27–251). After aging in H₂O + CO₂ atmosphere for 6 days, some Na⁺ ions are extracted from the bulk Na_{0.67}MnO₂ and the NaHCO₃ compound is formed, as demonstrated by the XRD and Fourier transformed infrared spectroscopy (FTIR) results in Fig. 3a, b. Simultaneously, H₂O is inserted into the Na⁺ layer, thus broadening the *c* parameter from 11.0 to 14.2 Å and transforming Na_{0.67}MnO₂ into the hydration phase (Fig. 3a, b)³⁴. SEM images show that the particles' surfaces of hydration phase are coated by NaHCO₃ (Fig. 2 and Supplementary Fig. 3). Moreover, due to the large volume expansion during hydration (~30%)³⁴, the Na_{0.67}MnO₂ particle breaks into multiple two-dimensional nanoflakes that stack along the *c* axis (Fig. 2 and Supplementary Fig. 3). To obtain S-NMO, the hydration phase was stirred in distilled water for 10 min and then dehydrated at 160 °C for 1 h to remove the NaHCO₃ impurities and inserted H₂O molecules, respectively.

To verify whether NaHCO₃ and H₂O impurities have been successfully removed, multiple characterizations were carried out. As shown in Fig. 3a–c, the NaHCO₃ signals in XRD pattern (30.4° and 34.4°), FTIR spectrum (600–2000 cm^{–1}), and ²³Na MAS NMR spectra (0 ppm) of S-NMO disappear, suggesting that the NaHCO₃ impurity has been removed. The absence of O–H stretching signal at 2500–3500 cm^{–1} of FTIR spectrum of S-NMO (Fig. 3b) demonstrates that the water molecules have been also eliminated. According to our previous results³⁴, during the annealing processes, the hydrated Na_{0.67}MnO₂ undergoes NaHCO₃ decomposition and dehydration processes in the temperature range of ~30–130 °C. As shown in the thermogravimetric analysis (TGA) results (Supplementary Fig. 4), no mass loss is observed during 30–300 °C of S-NMO, indicating that NaHCO₃ and H₂O have

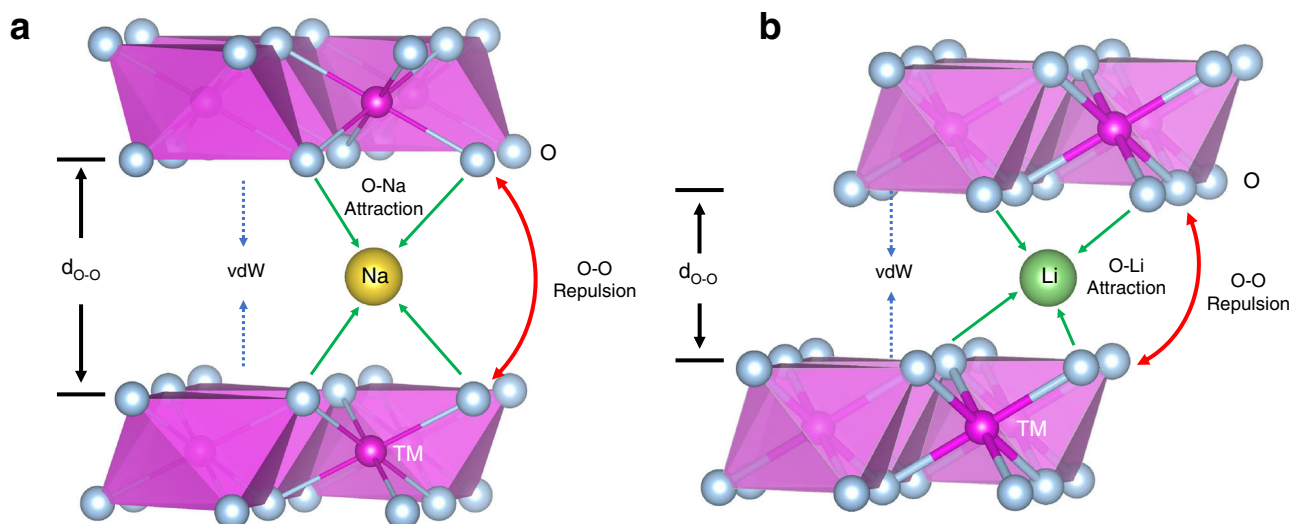


Fig. 1 Electrostatic interactions. Schematic illustration of the electrostatic interactions of **a** Na_xTmO_2 and **b** LiTmO_2 .

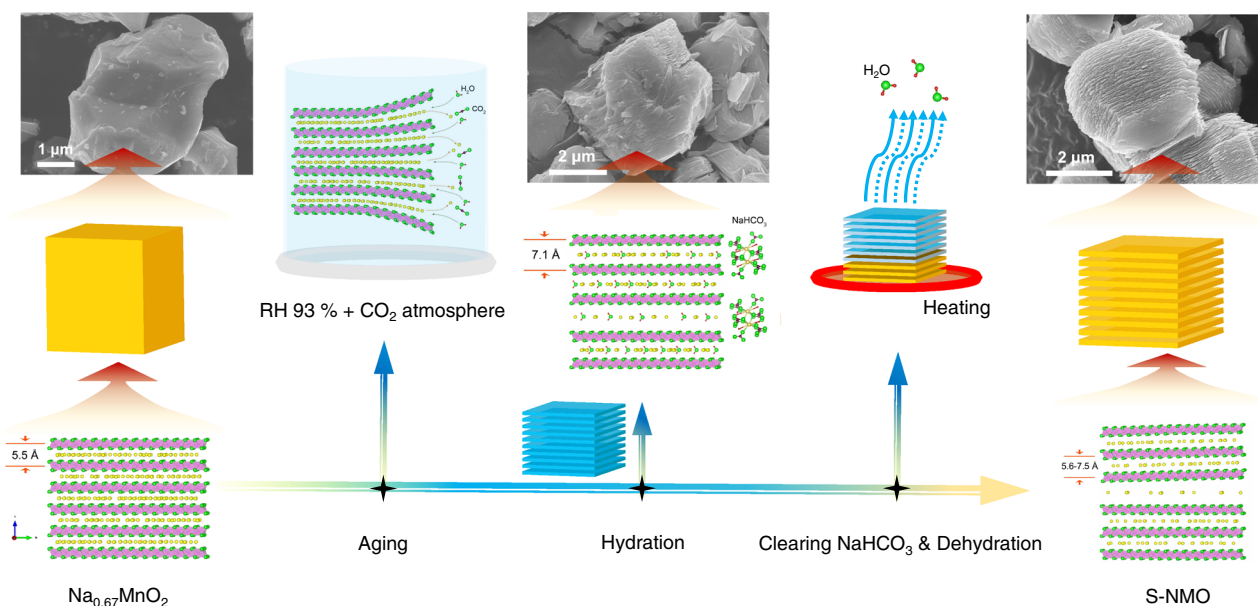


Fig. 2 Water-mediated strategy. Schematic illustration of the preparation process of S-NMO.

been removed (Supplementary Note 1), which coincides well with the XRD and FTIR results. In addition, $^{23}\text{Na}\{^1\text{H}\}$ rotational-echo double-resonance (REDOR) spectroscopy was used to inspect the residual protons (H^+) in S-NMO³⁴. The shift of ^{23}Na signal from 91.6 ppm of hydration phase to 1051 ppm of S-NMO corresponds to the contraction of the Na^+ layer spacings due to the dehydration process. For hydration phase (Fig. 3c), the $^{23}\text{Na}\{^1\text{H}\}$ REDOR-dephased signal intensities with ^1H pulses decrease as the spin-echo time increases from 0.93 to 1.60 ms as opposed to that without ^1H pulses, indicating the existence of protons in Na^+ layers. For S-NMO material, both $^{23}\text{Na}\{^1\text{H}\}$ REDOR-dephased signals with and without ^1H pulses at different spin-echo times remain the same, implying that no hydrogen atoms either in proton or H_2O states reside closely to the Na^+ . The above results demonstrate that NaHCO_3 , H_2O , and inserted protons have been successfully removed from S-NMO electrode.

SEM (Fig. 3h) and TEM (Supplementary Fig. 5) images confirm that the S-NMO is composed of two-dimensional

nanoflakes and the thickness of each nanoflake is about 10–30 nm. Inductively coupled plasma-atomic emission spectrometry (ICP-AES, Supplementary Table 1) reveals that the chemical composition of S-NMO is $\text{Na}_{0.21}\text{MnO}_2$. As shown in Fig. 3a and Supplementary Fig. 7, compared to the XRD pattern of pristine $\text{Na}_{0.67}\text{MnO}_2$, the (002) reflection of S-NMO asymmetrically broadens, ranging from 15.8° to 11.8° (2θ , $\text{Cu K}\alpha$ radiation), which corresponds to the lattice parameter c of 11.2–15.0 Å (3.8–5.8 Å for Na^+ layer spacing), much larger than that of $\text{Na}_{0.67}\text{MnO}_2$ (11.0 Å for c and 3.6 Å for Na^+ layer spacing). Simultaneously, (100) diffraction peak shifts from 36.18° (pristine $\text{Na}_{0.67}\text{MnO}_2$) to 36.54° (S-NMO), demonstrating that the lattice parameter a shrinks from 2.864 to 2.837 due to the oxidation of Mn ions. Moreover, because of the expansion of Na^+ layers, all of the (hkl) ($l \neq 0$) peaks broaden and lose their intensity, such as (004), (011), and (112), while the ($hk0$) peaks, such as (100) and (110), shift slightly to higher angles and maintain their intensity.

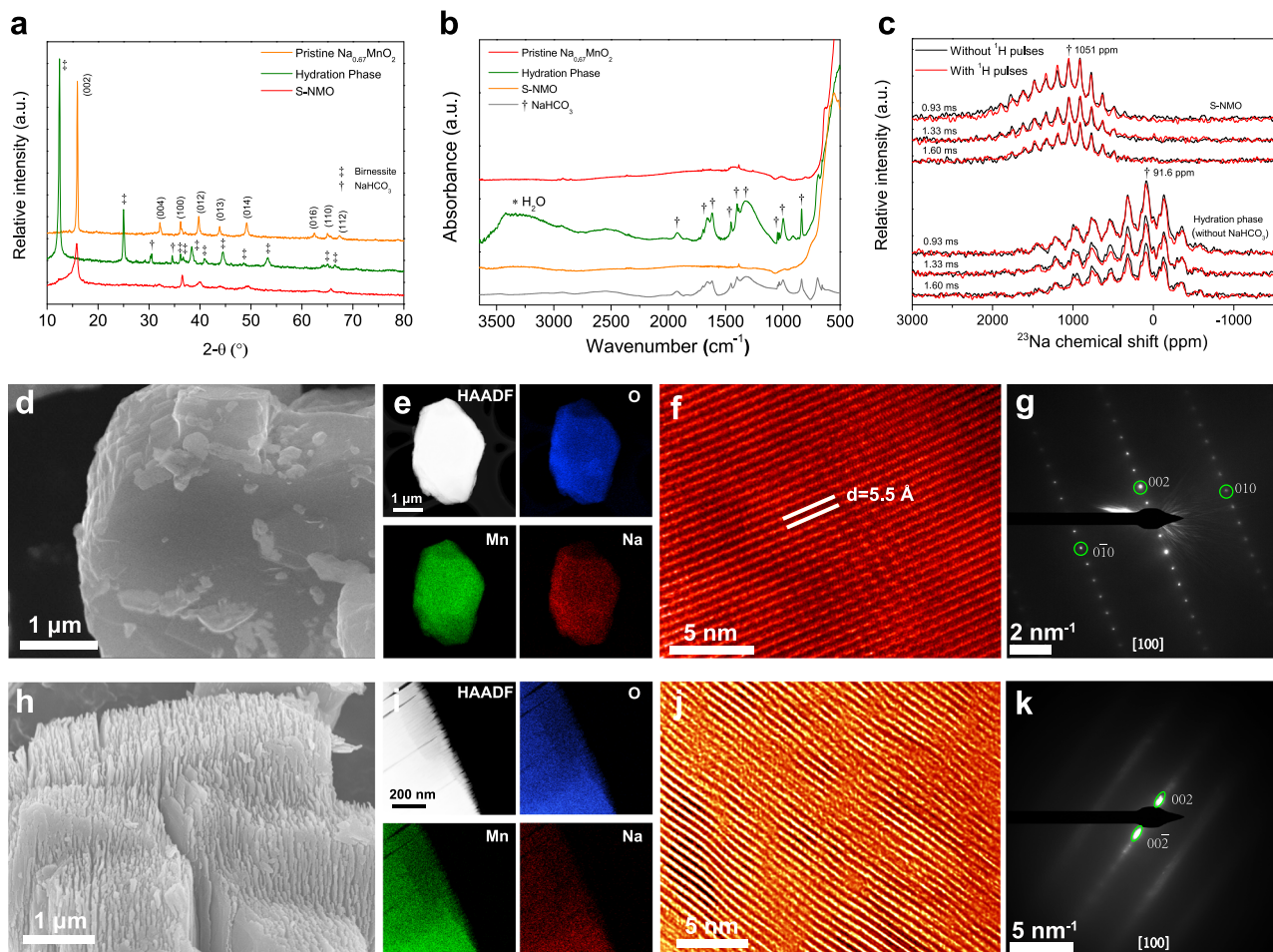


Fig. 3 Structural characteristics of S-NMO. **a** XRD patterns and **b** FTIR spectra of pristine $\text{Na}_{0.67}\text{MnO}_2$, S-NMO, and hydration phase. **c** $^{23}\text{Na}\{^1\text{H}\}$ REDOR-dephased MAS NMR spectra of S-NMO and hydration phase. **d** SEM, **e** EDS mapping, **f** TEM, and **g** SAED results of pristine P2-type $\text{Na}_{0.67}\text{MnO}_2$ material. **h** SEM, **i** EDS mapping, **j** TEM, and **k** SAED results of S-NMO material.

The migration of Mn ions from Tm layers to Na^+ layers might also lead to the changes of diffraction peaks in the XRD pattern. Therefore, XRD simulations considering the interlayer migration of Mn ions and expansion of interlayer spacing were carried out in a separately way. In P2-type Na_xMnO_2 material, Na ions are located in two different prismatic sites, i.e., Na_e (1/3, 2/3, 3/4) and Na_f (0, 0, 1/4). When Mn ions migrate from Mn site (0, 0, 0) to Na_e sites, the relative intensities of (012) and (013) peaks become relatively stronger than (002) peak with the increment in the contents of migrated Mn ions (Supplementary Fig. 7a). When Mn ions migrate from Mn site to Na_f sites, the relative intensity of (004), (100), and (015) peaks become stronger with the increase of migrated Mn ions (Supplementary Fig. 7b). These trends do not fit the difference between the XRD patterns of pristine $\text{Na}_{0.67}\text{MnO}_2$ and S-NMO (Fig. 3a). In contrast, with the increase in the fractions of expanded Na layers, the relative intensities of (*hkl*) ($l \neq 0$) peaks decrease, while that of (*hk0*) peaks remain unchanged (Supplementary Fig. 8), and this fact coincides well with the experimental results.

The atomistic structure of Na_xMnO_2 has been illustrated (Supplementary Fig. 9) to clarify the change of XRD patterns. As it is observed, the (*hk0*) planes are perpendicular to the (002) plane and the intensities of (*hk0*) diffraction peaks are not influenced by the expansion of Na^+ layers. However, the inhomogeneous broadening of the (002) plane reduces the atomic ordering degree of (*hkl*) ($l \neq 0$) planes and results in the weakening of (*hkl*) ($l \neq 0$) diffraction peaks.

To further probe the structures of pristine $\text{Na}_{0.67}\text{MnO}_2$ (Fig. 3d) and S-NMO (Fig. 3h) materials, TEM characterization was carried out. Elemental mapping results (Fig. 3e, i) indicate that Na, Mn, and O elements are homogeneously distributed in both pristine $\text{Na}_{0.67}\text{MnO}_2$ and S-NMO materials. High-resolution TEM images (Supplementary Fig. 10a, c) and selected area electron diffraction (SAED) patterns (Supplementary Fig. 10b, d) show that the atomic ordering and hexagonal crystal symmetry of S-NMO along [001] direction are identical to that of Pristine $\text{Na}_{0.67}\text{MnO}_2$, suggesting that the atomic ordering along *c* axis is well preserved during the water-mediated treatment. As shown in Fig. 3f, the pristine $\text{Na}_{0.67}\text{MnO}_2$ presents the straight (002) lattice fringes with a uniform spacing of 5.5 Å. By contrast, the (002) planes of S-NMO are slightly curved with varied interplanar spacings (Fig. 3j), as also confirmed by the SAED patterns. Compared to the typical SAED pattern of $\text{Na}_{0.67}\text{MnO}_2$ along [100] direction (Fig. 3g), only (002) and (00 $\bar{2}$) reflections of S-NMO can be clearly identified (Fig. 3k), indicating a reduced atomic ordering in the (100) plane. Moreover, the (002) and (00 $\bar{2}$) spots in Fig. 3k are elongated toward the central (000) spot, corresponding to the varied (002) d-spacings with different expansion rates. Thus, both high-resolution TEM and SAED analyses confirm that the Na^+ layer spacings expand after the water-mediated treatment, well consistent with the XRD results. The above results reveal that the S-NMO exhibits typical shale-like structural features³⁵.

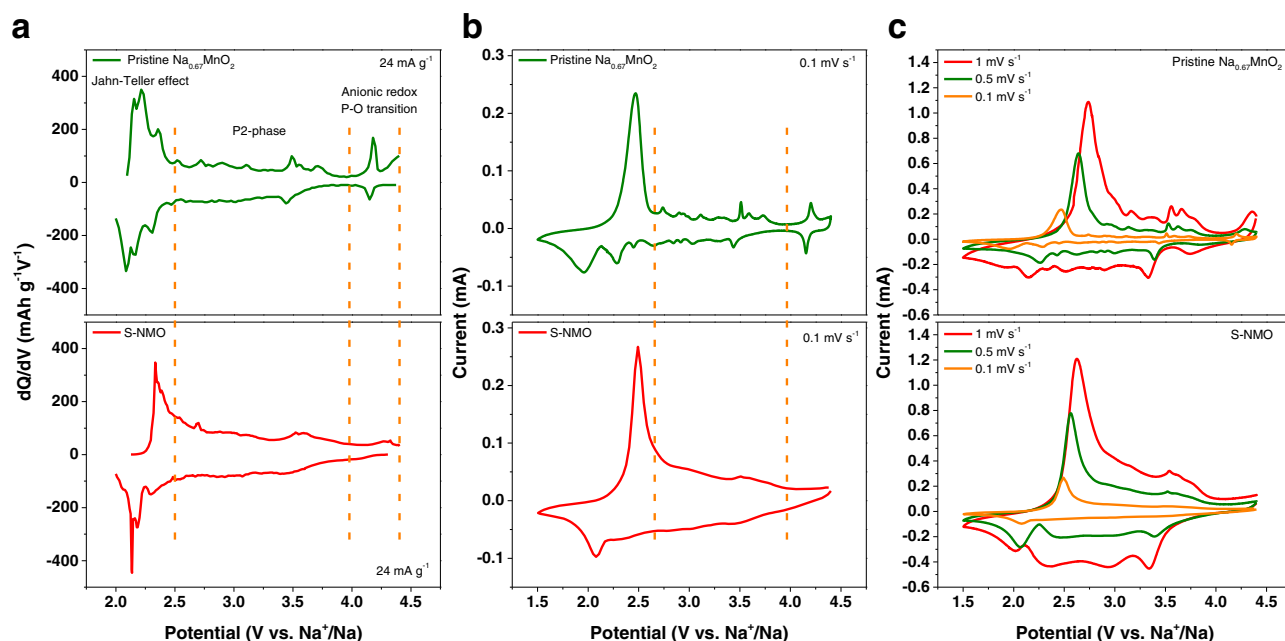


Fig. 4 Redox behavior of pristine $\text{Na}_{0.67}\text{MnO}_2$ and S-NMO. **a** dQ/dV profiles within 2.0–4.4 V obtained from galvanostatic curves at 24 mA g^{-1} . **b** CV curves at 0.1 mV s^{-1} from 1.5 to 4.4 V. **c** CV curves at the sweep rates of 0.1, 0.5, and 1 mV s^{-1} within 1.5–4.4 V.

Besides the structural changes at the lattice level, the change of particle size during water-mediated process is also observed. As shown in Supplementary Fig. 11, the median particle sizes (D50) of pristine $\text{Na}_{0.67}\text{MnO}_2$, hydration phase, and S-NMO are about 5.5, 7.3, and 3.9 μm , respectively. The particle size is expanded by $\sim 32\%$ from pristine $\text{Na}_{0.67}\text{MnO}_2$ to hydration phase, which coincides well with the XRD patterns (Fig. 3a) and the previous results³⁴. Due to the repeated volume expansion and contraction during the water-mediated process, the particles split along the grain boundaries of $\text{Na}_{0.67}\text{MnO}_2$ polycrystal (Supplementary Fig. 12), thus resulting in the smaller D50 value of S-NMO than pristine $\text{Na}_{0.67}\text{MnO}_2$. The elimination of grain boundaries is beneficial to maintain the particle integrity during the electrochemical cycling processes.

Electrochemical performances of S-NMO. The Na-storage electrochemical characteristics of S-NMO electrode were carried out in sodium half-cells with 1 M NaPF_6 -98% + PC-2% fluor-ethylene carbonate (FEC) solution as electrolytes.

To explore the redox behavior of pristine $\text{Na}_{0.67}\text{MnO}_2$ and S-NMO, the dQ/dV plots and cyclic voltammetry (CV) curves have been obtained and shown in Fig. 4. According to the redox and phase transition mechanisms^{9,13,20,22}, the pristine $\text{Na}_{0.67}\text{MnO}_2$ electrode can be briefly separated into three regions: anionic redox region, P2-phase region, and Jahn–Teller distortion region. The anionic redox reactions occur at ~ 4.0 – 4.4 V, which are usually accompanied by P–O phase transitions^{9,20}. At ~ 2.5 – 4.0 V, the $\text{Na}_{0.67}\text{MnO}_2$ electrode shows P2 structure and exhibits fast kinetics and high redox reversibility^{20,22}. The redox peaks at this stage could be attributed to the local structural transitions of Na vacancy and $\text{Mn}^{3+}/\text{Mn}^{4+}$ orderings³⁶. Due to the $\text{Mn}^{3+}/\text{Mn}^{4+}$ redox reaction, the Jahn–Teller distortion occurs at the voltages below 2.5 V, which has been also termed as P2-P2' phase transformation¹³.

As compared to pristine $\text{Na}_{0.67}\text{MnO}_2$, the S-NMO electrode shows much smoother dQ/dV plots and CV curves, indicating the local structural transitions of $\text{Na}_{0.67}\text{MnO}_2$ are mitigated. Moreover, as shown in Fig. 4a, b, the contribution of specific capacity by the anionic redox reactions and Jahn–Teller distortion regions decreases after the water-mediated treatment. As shown in Fig. 4c, the

overpotential of $\text{Mn}^{3+}/\text{Mn}^{4+}$ and anionic redox reactions of pristine $\text{Na}_{0.67}\text{MnO}_2$ electrode increases drastically on increasing the scan rates. At the scan rates of 0.1, 0.5, and 1 mV s^{-1} , the anodic peaks of $\text{Mn}^{3+}/\text{Mn}^{4+}$ redox couple of pristine $\text{Na}_{0.67}\text{MnO}_2$ increase from 2.46 to 2.64 and 2.74 V, respectively, and the potential polarization of anionic redox reactions increases from 0.05 V (4.20/4.15 V) to 0.42 (4.28/3.86 V) and 0.61 V (4.35/3.74 V), respectively, demonstrating the slow kinetics of both $\text{Mn}^{3+}/\text{Mn}^{4+}$ and anionic redox reactions. By contrast, the anodic peaks of $\text{Mn}^{3+}/\text{Mn}^{4+}$ redox couple of the S-NMO electrode are located at the lower voltages of 2.47, 2.56, and 2.61 V at the scan rates of 0.1, 0.5, and 1 mV s^{-1} , respectively.

Furthermore, to check the capacitive contributions in both NMO and S-NMO electrodes, we analyzed the anodic peaks located at ~ 2.5 V ($\text{Mn}^{3+}/\text{Mn}^{4+}$ redox peak) and 3.5 V as³⁷

$$i = av^b \quad (1)$$

where i corresponds to the current densities at various scan rates (v , mV s^{-1}) and a and b are adjustable constants. When the b value approaches 0.5 and 1, the redox reactions tend to be diffusion-controlled or surface-controlled, respectively^{38,39}. As shown in Supplementary Fig. 16, the b value of NMO and S-NMO electrodes at 2.5 V are 0.60 and 0.69, respectively, which suggests a diffusion-controlled characteristic for $\text{Mn}^{3+}/\text{Mn}^{4+}$ redox reactions. When the potential increases to 3.5 V (Supplementary Fig. 17), the b value increases to 0.67 and 0.89 for NMO and S-NMO electrodes, respectively. Compared to the NMO electrode, the S-NMO electrode exhibits greater surface faradaic contribution due to the open morphology (Fig. 3h).

According to the CV results, the ameliorated electrochemical polarization of S-NMO could be attributed to the improved reaction kinetics, the increased surface faradaic capacity contribution, and more favorable pathways for Na^+ diffusion because of the expanded Na^+ layers spacings.

To further understand the differences between pristine $\text{Na}_{0.67}\text{MnO}_2$ and S-NMO, electrochemical impedance spectroscopy (EIS) measurements were carried out. Supplementary Fig. 13 shows the Nyquist plots of pristine $\text{Na}_{0.67}\text{MnO}_2$ and S-NMO electrodes at the discharged 2.8 V states^{20,40}. The ohmic

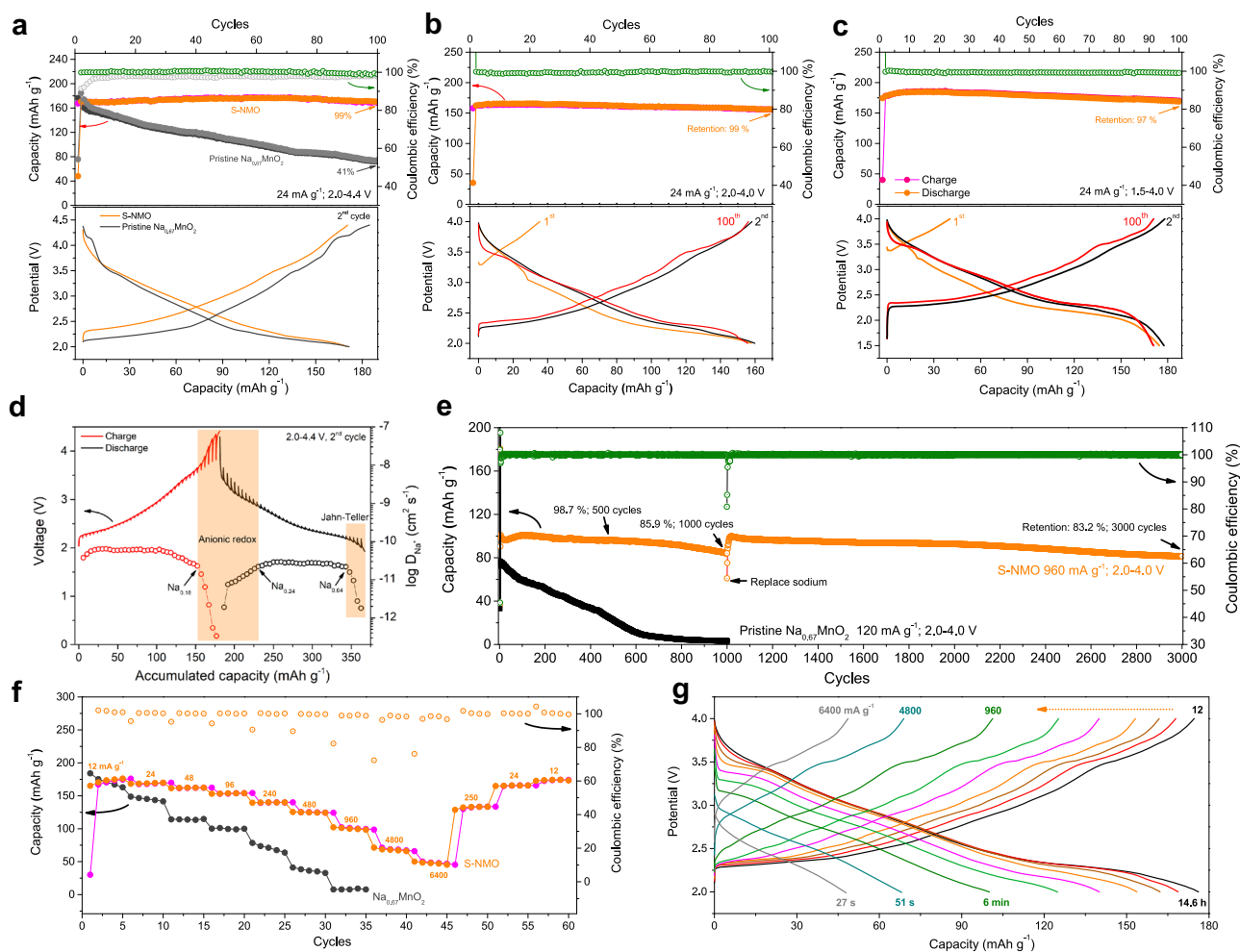


Fig. 5 Electrochemical performances of S-NMO. The cycling performances and charge–discharge curves of S-NMO electrode at 24 mA g^{-1} within the voltage ranges of **a** 2.0–4.4 V, **b** 2.0–4.0 V, and **c** 1.5–4.0 V. **d** GITT results of S-NMO electrode. **e** The comparison of the cycling performance of pristine $\text{Na}_{0.67}\text{MnO}_2$ and S-NMO electrodes at 120 and 960 mA g^{-1} , respectively. **f** The rate performance of pristine $\text{Na}_{0.67}\text{MnO}_2$ and S-NMO at the voltage range of 2.0–4.0 V. **g** The charge–discharge profiles of S-NMO at different current densities.

resistances (R_{ohm}) of pristine $\text{Na}_{0.67}\text{MnO}_2$ and S-NMO are 25.4 and 27.8Ω , respectively, implying the water-mediated strategy is beneficial for enhancing the electronic conductivity. At the medium- and high-frequency region (1 Hz–100 kHz), the electrode impedances consist of charge transfer resistances and surface resistances of both cathode and anode ($R_{\text{CT}+\text{SR}}$). As shown in Supplementary Fig. 13, the $R_{\text{CT}+\text{SR}}$ of S-NMO is lower than pristine $\text{Na}_{0.67}\text{MnO}_2$, demonstrating the faster kinetic of redox reactions of S-NMO than pristine $\text{Na}_{0.67}\text{MnO}_2$.

As shown in Fig. 5a, the S-NMO electrode shows improved coulombic efficiency and smoother charge–discharge profiles than pristine $\text{Na}_{0.67}\text{MnO}_2$ ^{20,41}. At the current density of 24 mA g^{-1} (0.2 C) within the voltage range of 2.0–4.4 V, the pristine $\text{Na}_{0.67}\text{MnO}_2$ electrode exhibits rapid capacity decay with only 41% capacity retention after 100 cycles. At the same testing conditions, S-NMO electrode shows no obvious capacity decay (Fig. 5a). At the potential ranges of 2.0–4.0 V (Fig. 5b), 2.0–4.4 V (Fig. 5a), and 1.5–4.0 V (Fig. 5c), the delivered specific capacities of S-NMO electrode at 0.2 C (24 mA g^{-1}) are 162, 170, and 181 mAh g^{-1} , and the corresponding capacity retentions after 100 cycles are 99%, 99%, and 97%, respectively. No obvious capacity and voltage decay are observed in the charge–discharge profiles of 2nd, and 1000th cycles (Fig. 5b, c), demonstrating the excellent cycling stability of S-NMO electrode.

To investigate the kinetic characteristics of the S-NMO electrode, we carried out the galvanostatic intermittent titration technique (GITT) analysis and calculated the corresponding diffusion coefficients of Na^+ (D_{Na^+})⁴⁰. As shown in Fig. 5d, the D_{Na^+} of S-NMO at the voltage range of 2.0–3.5 V remains stable with the geomean D_{Na^+} value of $5.1 \times 10^{-11} \text{ cm}^2 \text{ s}^{-1}$. When the sodium contents of S-NMO decrease from 0.18 to 0.08 (the end of charge), the D_{Na^+} value decreases rapidly from 2.28×10^{-11} to $3.33 \times 10^{-13} \text{ cm}^2 \text{ s}^{-1}$, probably resulted from the increased electrostatic interactions of $\text{Na}^+\text{-O}$ bonds and the slower reaction kinetics of possible anionic redox reactions. At the initial stage of the discharge process, the D_{Na^+} value increases gradually and reaches $2.2 \times 10^{-11} \text{ cm}^2 \text{ s}^{-1}$ at the sodium content of 0.24. Then, the D_{Na^+} value remains constant with the geomean value of $2.64 \times 10^{-11} \text{ cm}^2 \text{ s}^{-1}$ until the sodium content reaches 0.64. Due to the Jahn–Teller effects and increased $\text{Na}^+\text{-Na}^+$ electrochemical interactions, the D_{Na^+} value decreases from 2.18×10^{-11} to $1.8 \times 10^{-12} \text{ cm}^2 \text{ s}^{-1}$ at the end of the discharge process. The more sluggish diffusion of Na^+ during anionic redox reactions and Jahn–Teller transitions demonstrate that the capacity delivered at the high current densities mainly originates from the sodium contents of 0.2–0.65 ($\sim 130 \text{ mAh g}^{-1}$). Compared to P2-type $\text{Na}_{0.67}\text{MnO}_2$, the calculated geomean D_{Na^+} values of S-NMO are 11 times higher during the charge process and 2 times higher during the discharge process²⁰.

As shown in Fig. 5e, at 120 mA g⁻¹, the specific capacity of pristine Na_{0.67}MnO₂ electrode reduces to only 4% (3 mAh g⁻¹) of the initial capacity after 1000 cycles. Moreover, the CV curves in Supplementary Fig. 14 show that both the cathodic and anodic peaks disappear, revealing the complete collapse of the pristine Na_{0.67}MnO₂ electrode. In contrary, the S-NMO electrode exhibits an initial discharge capacity of 98 mAh g⁻¹ at 960 mA g⁻¹ (8 C, 2.0–4.0 V). After 500 and 1000 cycles, 99 and 86% of the initial capacity is maintained, respectively (Fig. 5e). As shown in Supplementary Fig. 15, the redox characteristics of S-NMO during the charge process remain almost unchanged except for the slight shift of the redox peaks and the minor capacity degradation, demonstrating that the redox behavior of S-NMO is well maintained after 1000 cycles.

To investigate the degradation mechanisms of S-NMO electrodes during long cycling, the top-view SEM images of S-NMO electrodes before and after 1000 cycles have been obtained. As shown in Supplementary Fig. 18a, b, the pristine S-NMO electrode is composed of conductive carbon and S-NMO particles. After 1000 cycles (Supplementary Fig. 18c, d), the surface of the S-NMO electrode is covered by a cathode electrolyte interphase (CEI) layer, suggesting the electrolyte decomposition might be the main cause that leads to the degradation of S-NMO electrode. Therefore, we assembled a new half-cell based on the cycled S-NMO electrode. As shown in Fig. 5e, after replacing with a fresh electrolyte and sodium counter electrode, the S-NMO electrode recovers to 99 mAh g⁻¹ at 960 mA g⁻¹ and retains 94 and 83% of the original capacity after 2000 and 3000 cycles, respectively. In addition, Supplementary Fig. 19 shows that the charge–discharge profiles of S-NMO over 3000 cycles at 960 mA g⁻¹ remain practically unchanged, revealing the excellent structural stability during long cycling.

Figure 5f compares the rate performances of Na_{0.67}MnO₂ and S-NMO electrodes within 2.0–4.0 V. At the current density of 12 mA g⁻¹ (0.1 C), S-NMO delivers a high specific capacity of 175 mAh g⁻¹, which is comparable to that of Na_{0.67}MnO₂. When the current density increases by 4-, 8-, 20-, 40-, and 80-folds, S-NMO maintains 92%, 87%, 80%, 71%, and 57% (100 mAh g⁻¹) of the capacity delivered at 12 mA g⁻¹, respectively. In contrast, the specific capacity of Na_{0.67}MnO₂ degrades rapidly at the first ten cycles at 12 and 24 mA g⁻¹. At the current densities of 960 mA g⁻¹ (8 C), S-NMO electrode delivers 12.5-folds of specific capacity of Na_{0.67}MnO₂, demonstrating a greatly improved rate performance after the water-mediated strategy. The charge–discharge profiles of S-NMO electrode at various current densities ranging from 12–6400 mA g⁻¹ are shown in Fig. 5g, showing that high specific capacities of 100, 68, and 47 mAh g⁻¹ can be achieved even at the very short operation time of 6 min, 51 s, and 27 s, respectively.

The above electrochemical performances reveal excellent electrochemical reversibility and structural stability of S-NMO electrode, demonstrating lattice engineering is a promising strategy for layered oxide cathodes. With further electrode/electrolyte modifications, such as doping, coating, oxide-carbon composites, or electrolyte modulations, the S-NMO will become a promising cost-effective NIBs electrode for practical applications.

The structural evolutions of S-NMO during charge and discharge. Layered oxide cathodes usually undergo various phase transformations during charge–discharge processes. For example, Na_{0.67}MnO₂ experiences C2/c-P2, P2-P2', and P2-OP4 phase transformations thus resulting in electrode degradations and capacity decay^{13,20,22}. To unravel the origin of the improved electrochemical performances of S-NMO electrode, in situ lab-

source/synchrotron XRD and ²³Na MAS NMR were performed to investigate the structural transformations during cycling.

Firstly, in situ lab-source XRD patterns with Cu K α radiation ($\lambda = 1.5405 \text{ \AA}$) are recorded. As shown in Supplementary Fig. 20, the shift and intensity changes of (002) peak are negligible during the charge–discharge processes. Other diffraction peaks, such as (004), (100), (103), and (104) are also found in the in situ XRD patterns, but their intensities are too low to be analyzed due to the structural changes during the water-mediated process (Fig. 3a). Synchrotron X-ray is much brighter than the lab-source X-ray. Moreover, the transmission mode of the in situ synchrotron XRD setup strengthens the intensity of (*hkl*) (*h* + *k* \neq 0) diffraction peaks⁹. Therefore, in situ synchrotron XRD ($\lambda = 0.6887 \text{ \AA}$) was further utilized to track the structural changes of S-NMO.

The in situ synchrotron XRD patterns and the corresponding contour map are shown in Fig. 6a, b, respectively. No new peak appears, indicating that the P2 structure is well maintained during the whole charge–discharge processes. Both position and intensity of the (002) diffraction peak remain static during the initial two cycles, which coincides well with the in situ lab-source XRD patterns. The other diffraction peaks, including (100), (110), (102), and (112), contract during charge and expand during discharge because of the oxidation and reduction of Mn ions, respectively. The variations in lattice parameters and volume during the first two cycles were calculated (Fig. 6c and Supplementary Note 2). During the charge process, the parameter *c* of Mn-based layered sodium oxides usually increases firstly and then contracts, due to the increased repulsion of adjacent oxygen layers and the following glides of TmO₂ slabs^{13,22}. As shown in Fig. 6c, parameter *c* remains unchanged and the lattice parameter *a* and volume (*V*) experience maximum changes of 0.98% and 1.96%, respectively, demonstrating a near-zero-strain insertion/extraction property during charge–discharge process. The volume change of S-NMO electrode is larger than that of the zero-strain Li₄Ti₅O₁₂⁴² due to the redox reaction of Mn ions. However, it is much smaller than that of the typical commercial cathodes for LIBs, such as LiMn₂O₄ (*V*: ~5.6%)⁴¹, 4.3 V LiCoO₂ (*c*: ~2.6%)⁴³ and LiFePO₄ (*V*: ~6.8%)⁴⁴, which explains the outstanding electrochemical performances of S-NMO electrode.

The structural transformations during the first and second cycles were further studied by ex situ ²³Na MAS NMR. As shown in Fig. 6d, the NMR signals that are located at 0, 200–500, 800–900, and 900–1450 ppm correspond to the Na⁺ in diamagnetic sodium salts (such as CEI), hydration, P2' (Mn³⁺-rich environment), and P2 phases, respectively, and the signals located at 1700–1900 ppm most probably arise from the Mn⁴⁺-rich local environments^{19,20,22}. Trace amounts of hydration phase at the discharged 3.75 V state of the first cycle and the charged 4.0 V state of the second cycle are introduced during the cell disassembling processes.

The NMR spectrum of pristine S-NMO electrode shows two signals located at 1813 and 1143 ppm, corresponding to the local Mn⁴⁺-rich and P2 environments, respectively^{20,22,45}. During the charge process, the intensities of two signals decrease progressively due to the extraction of Na⁺ from both P2-type and Mn⁴⁺-rich environments. During the discharge process within 4.4–2.25 V, these two signals become stronger gradually. With the further intercalation of Na⁺, Mn⁴⁺-rich local environment disappears and a new Mn³⁺-rich signal (i.e., local P2' phase) that is located at ~830 ppm emerges, corresponding to the reduction of Mn ions. At the start of the charge process of the second cycle, the local P2' phase disappears and the Mn⁴⁺-rich environment reappears. During the second charge process, the P2-phase signal keeps decreasing. Meanwhile, the signal of the Mn⁴⁺-rich environment gradually recovers before the voltage reaches 3.5 V and then becomes weaker with the further extraction of Na⁺. The P2'-type

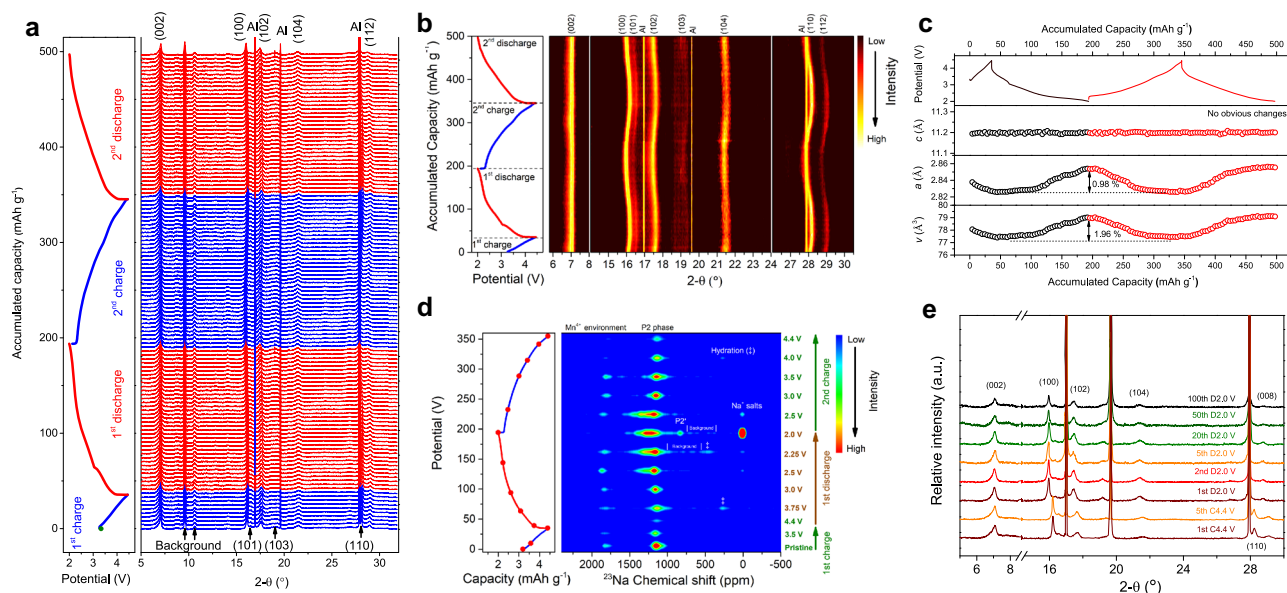


Fig. 6 Structural evolution mechanisms of S-NMO. **a** In situ XRD patterns, **b** in situ XRD contour map, **c** calculated lattice parameters, and **d** ex situ ^{23}Na MAS NMR spectra of S-NMO during the charge–discharge processes. **e** The comparison of XRD patterns of S-NMO at different cycles.

phase (Mn^{3+} -rich environment) appears in MAS NMR spectra at 2.0 V (Fig. 6d) but is absent in the observed in situ synchrotron XRD patterns (Fig. 6a), indicating the disruption of the long-range Jahn–Teller distortion by the water-mediated treatment.

To further probe the stability of S-NMO electrode, ex situ synchrotron XRD patterns at different cycles were studied, as shown in Fig. 6e. These electrodes are tested at the current density of 24 mA g^{-1} (0.2 C) within 2.0–4.4 V (Fig. 5a). Previous results indicate that the (002) diffraction peak of Mn-based layered sodium oxides shifts to a lower angle due to the irreversible redox reactions²⁰. As shown in Fig. 6e, at the charged 4.4 V state of both the first and the fifth cycles, all of the diffraction peaks fit well with the P2-type structure, indicating the P-type to O-type structural transformations are inhibited. At the discharged 2.0 V state of the 1st, 2nd, 5th, 20th, 50th, and 100th cycles, all of the diffraction peaks fit well with neither shift nor extra peaks can be observed, demonstrating the excellent structural reversibility under repeated Na^+ intercalation and extraction processes.

Altogether, the above XRD and NMR results demonstrate that the S-NMO electrode shows a near-zero-strain property with high structural and electrochemical reversibility during cycling.

Discussions

Due to the high abundance, cost-effectivity, and environmental friendliness, Mn-based layered sodium oxides possess the qualifications to meet the low-cost requirement of NIBs. However, the electrochemical performances of these promising electrodes are still far from satisfactory due to the Jahn–Teller effect and the migration of adjacent TmO_2 layers. The modifications of P2-type Na_xMnO_2 electrodes are mainly focused on doping (substitution), coating, and electrolyte modulation. In this work, by using a water-mediated method, we successfully expanded the Na^+ layer spacings of P2-type $\text{Na}_{0.67}\text{MnO}_2$, improved the structural stability and Na^+ mobility, and obtained the electrochemically stable S-NMO electrode.

The water-mediated strategy has been also applied in $\text{Na}_{0.67}\text{Zn}_{0.1}\text{Mn}_{0.9}\text{O}_2$ and $\text{Na}_{0.67}\text{Fe}_{0.1}\text{Mn}_{0.9}\text{O}_2$ materials to verify its feasibility on other layered sodium oxides. As shown in Fig. 7a, b, similar shale-like structure with accordion-like morphologies of S-NMO are observed for treated $\text{Na}_{0.67}\text{Zn}_{0.1}\text{Mn}_{0.9}\text{O}_2$ (S-NZMO) and $\text{Na}_{0.67}\text{Fe}_{0.1}\text{Mn}_{0.9}\text{O}_2$ (S-NFMO) materials. At the current

density of 24 mA g^{-1} within 2.0–4.0 V, the delivered discharge capacities of S-NZMO and S-NFMO electrodes are 140 and 144 mAh g^{-1} , respectively, with 99% and 98% of the original discharge capacities retained after 100 cycles, much better than the pristine electrodes. As shown in Fig. 7c, the S-NZMO and S-NFMO electrodes show similar charge–discharge curves as S-NMO with smooth slope within 2.0–4.0 V.

Air stability is an important criterion to evaluate a qualified electrode material. Therefore, a survey of moisture tolerance of S-NMO electrode was conducted by FTIR and the results are shown in Fig. 7d. After aging S-NMO in RH 93% + CO_2 for 3 days, the O–H stretching signal located at $3000\text{--}3500 \text{ cm}^{-1}$ emerges, suggesting that the S-NMO is hydrated at the moist atmosphere. The absence of Na_2CO_3 and NaHCO_3 characteristic peak at $600\text{--}2000 \text{ cm}^{-1}$ suggests that Na^+ in S-NMO is highly stable. After dehydrating the hydrated S-NMO material at 160°C in air for 2 h, the FTIR spectrum of re-dehydrated S-NMO material fits well with that of pristine S-NMO with neither O–H stretching signal nor NaHCO_3 appears (Fig. 7d), indicating the hydrated S-NMO can be easily recovered by mild annealing process. The above results suggest that the S-NMO material has excellent moisture tolerance and can be stored at ambient atmospheres.

In summary, a S-NMO electrode has been developed by a water-mediated method. This electrode exhibits outstanding electrochemical performances and excellent structural stability with near-zero-strain property. Notably, the S-NMO electrode shows superior moisture tolerance. It can be stored in highly humid environments and lowers the cost of the preparation and storage of layered sodium oxides. Furthermore, the feasibility of this water-mediated strategy to other layered transition metal oxides is validated. This work presents a simple but effective strategy to eliminate the phase transformations of Na_xTmO_2 and provides new guidelines for future design in reining the structure of layered transition metal cathodes.

Methods

Preparation of pristine layered sodium oxides. The pristine $\text{Na}_{0.67}\text{MnO}_2$, $\text{Na}_{0.67}\text{Fe}_{0.1}\text{Mn}_{0.9}\text{O}_2$, and $\text{Na}_{0.67}\text{Zn}_{0.1}\text{Mn}_{0.9}\text{O}_2$ samples were synthesized via high-temperature solid-state reaction⁴⁰. Stoichiometric amounts of MnO_2 (99.95%, Aladdin), Na_2CO_3 (99.99%, Aladdin), Fe_2O_3 (99.95%, Aladdin), and ZnO (99.99%, Aladdin) were

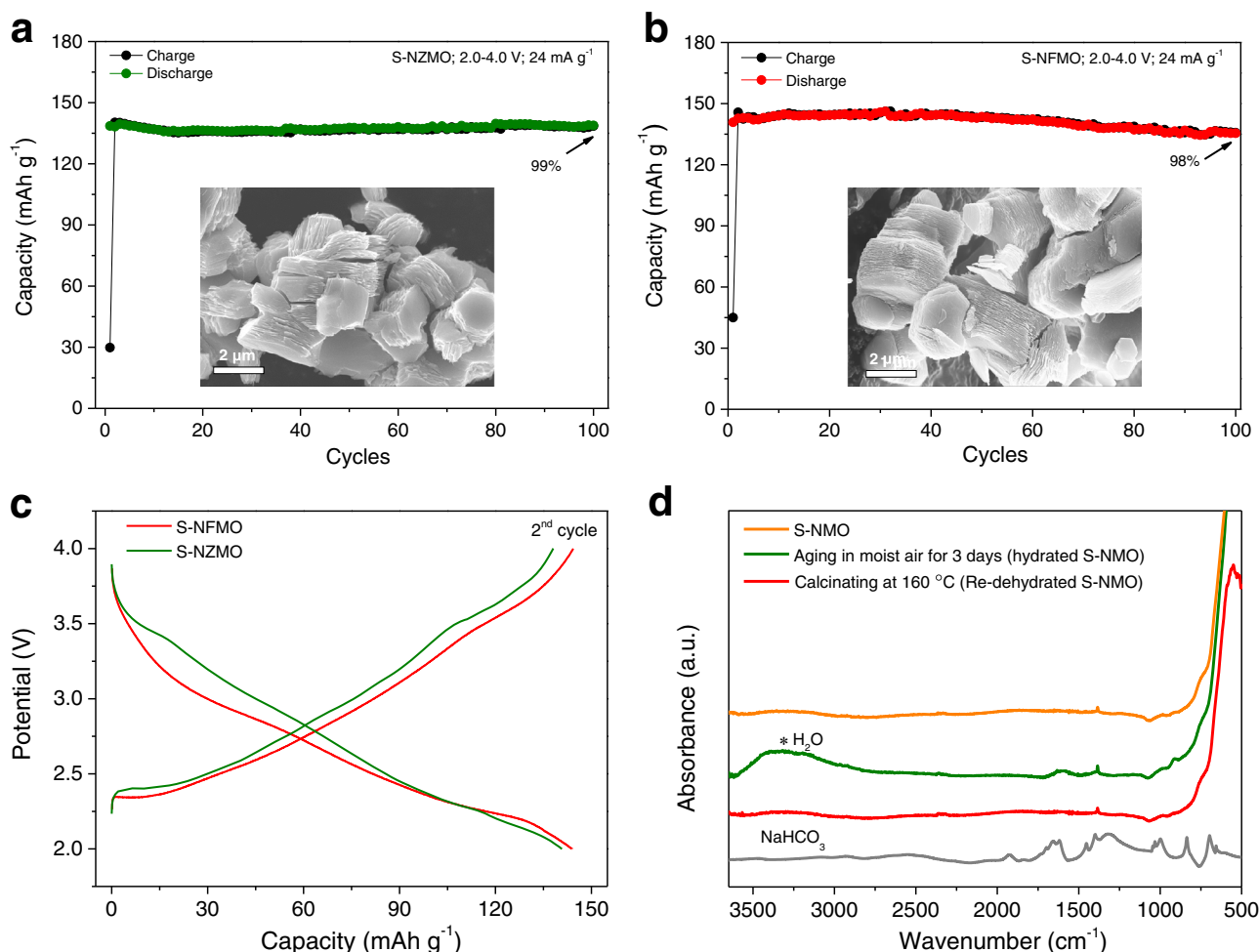


Fig. 7 Merits of the water-mediated method. The morphologies and cycling stability of **a** S-NZMO and **b** S-NFMO. **c** Charge-discharge curves of S-NFMO and S-NZMO within the voltage range of 2.0–4.0 V. **d** FTIR spectra of S-NMO, hydrated S-NMO, and re-dehydrated S-NMO.

mixed homogeneously by ball milling with acetone at 350 rpm min^{-1} for 12 h. The mixture was dried at 120°C for 12 h, pressed into pellets, and then sintered at 900°C for 15 h in air. The pellets were removed to Ar-filled glove box at 150°C , ground into powder, and stored in the Ar-filled glove box.

Preparation of Shale-like layered sodium oxides. To prepared Shale-like layered sodium oxides, the above synthesized powder was aged on the atmosphere of relative humidity of 93% with the presence of CO_2 (RH 93% + CO_2) at 40°C for 6 days³⁴. One gram of exposed sample was stirred in 30 mL distilled water for 10 min at room temperature, centrifuged and washed with ethanol, dried at 120°C for 6 h, and dehydrated at 160°C for 12 h. The final samples were stored at Ar-filled glove box.

Theoretical calculations. The interaction potential energies between one atom of x and multiple (N) atoms of y were calculated via Eq. (2). During the calculation, we regard Na and O as point charges with charge amounts of $+q$ and $-2q$, respectively

$$U_{x-y} = \sum_{i=1}^N \frac{q_x q_{yi}}{4\pi\epsilon_0 r_i} \quad (2)$$

where $x = \text{Na1}$, O1 and $y = \text{O2}$ (Supplementary Fig. 1a). U_{x-y} represents the interaction energy between atoms x and y ; q_x , q_{yi} , and r_i correspond to the charge of the x atom, the charge of the y atom, and the distance between the x and y_i atoms, respectively; N is the amounts of y atoms whose distance to the x atom is lower than 10 \AA .

The plane-wave PAW DFT calculations (Supplementary Fig. 2) were carried out by the Vienna ab initio Simulation Package^{46,47} with the Perdew–Burke–Ernzerhof functional (GGA-PBE) formula⁴⁸. The cutoff energy of 500 eV was employed and the SCF convergence energy was set to 10^{-7} eV . DFT+U method was adopted and the U_{eff} of Mn 3d states were set to 4.9 eV . The Brillouin zone was sampled with $7 \times 7 \times 2$ Monkhorst-Pack grids. In addition, vdW-DF2 was used to

calculate vdW energy⁴⁹. The layer spacing $d_{\text{O-O}}$ is adjusted in the range of $1.5\text{--}7 \text{ \AA}$. The vdW energy at the d-spacings of Na^+ layers ($d_{\text{O-O}}$) of 50 \AA was set to 0 eV .

Characterizations. The powder XRD patterns were collected on a BrukerD8 Discover A25 diffractometer with $\text{Cu K}\alpha$ radiation ($\lambda = 1.5406 \text{ \AA}$) at a scanning rate of 8° min^{-1} . XRD simulation was performed via CrystalMaker (version 2.3.2) with the structure of P2-type $\text{Na}_{0.2}\text{MnO}_2$ (space group: $P6_3/mmc$)^{13,20,22}. The SEM images of prepared samples were characterized by Hitachi S-4800 (HITACHI, Japan) microscope and Zeiss Sigma 300. The high-resolution TEM, energy dispersive X-ray spectroscopy (EDS) elemental mapping, and SAED experiments were conducted via FEI Talos-F200s TEM instrument. The composition of samples was tested via ICP-AES (Iris Intrepid II XSP, Thermo Electron). The ^{23}Na ss-NMR spectra were acquired on a Bruker AVANCE III 400 MHz spectrometer using a double-resonance 1.3 mm MAS probe at a spinning rate of 55 kHz with a Hahn-echo pulse sequence ($90^\circ \text{ pulse} - \tau - 180^\circ \text{ pulse} - \tau$). The 90° pulse length for ^{23}Na was $1.2 \mu\text{s}$ and the recycle delay was 2 ms . The ^{23}Na shifts were referenced to 1 M NaCl aqueous solution (0 ppm). The REDOR NMR sequence⁵⁰ is applied to confirm the existence of H_2O and H^+ in the prepared materials. Geometry-independent information about the dipole couplings between the observation nuclear species S (^{23}Na) and the heteronuclear species I (^1H) can be conveniently obtained from the experimental curve of the signal attenuation (1-scale) versus dipolar evolution time (T). FTIR spectra were recorded on a Nicolet is50 FTIR (Thermo Fisher Scientific Inc., Madison, USA) spectrometer. TGA experiments were performed in a STA 409 PC analyzer (Netzsch).

In situ XRD. All of the in situ XRD experiments were performed at room temperature with 2025-type coin cell within $2.0\text{--}4.45 \text{ V}$. Lab-source in situ XRD experiments were carried out on a BrukerD8 Discover diffractometer that equipped with a $\text{Cu K}\alpha$ radiation. In situ synchrotron XRD patterns were acquired at BL14B1 of the Shanghai Synchrotron Radiation Facility (SSRF)⁵¹. A monochromatic X-ray beam with an energy of 18 keV ($\lambda = 0.6887 \text{ \AA}$) and a beam size of $180 \mu\text{m}$ (width) $\times 200 \mu\text{m}$ (height) was adopted. The Mythen 1 K linear detector was

adapted for high-resolution powder diffraction data acquisition in Debye–Scherrer mode. The wavelength of the X-ray was calibrated using LaB₆ standard from NIST (660b). The diffraction peaks' FWHM of standard LaB₆ is less than 0.02°⁵². The lattice parameters were calculated according to Bragg equation

$$2d \sin \theta = n\lambda (\lambda = 0.6887 \text{ \AA}) \quad (3)$$

Specifically, *a* and *c* were obtained based on the position (2θ) of (100) and (002) diffraction peaks, respectively. The position at the highest intensity of (002) diffraction peak has been selected to calculate the lattice parameter *c* (Supplementary Note 2).

Electrochemical tests. The sodium half-cells were assembled in Ar-filled glove box with 1 M NaPF₆ in propylene carbonate (PC, 98 vol%) and fluoroethylene carbonate (2 vol%) as the electrolyte and Whatman glass fiber filter as the separator. The cathodes were composed of 10 wt% acetylene carbon black, 80 wt% of active materials (layered oxides), and 10 wt% of polyvinylidene fluoride. The mass loading of active materials was ~3 mg cm⁻². The electrochemical testing (galvanostatic charge–discharge and GITT) of sodium-ion half-cells were performed at 30 °C using LAND battery testing system (CT2001A, Wuhan, China) in 2025-type coin cells. The GITT of the S-NMO at the second cycle was applied by charging and discharging the testing cell at 9 mA g⁻¹ for 20 min, and then relax it for 1 h. The Na⁺ diffusion coefficient was calculated as

$$D_{\text{Na}^+} = \frac{4}{\pi\tau} \left(\frac{m_b V_m}{M_b A} \right) \left(\frac{\Delta E_s}{\Delta E_r} \right) \quad (4)$$

where *m_b*, *M_b*, *V_m*, and *A* correspond to the electrode mass, molecular weight, molar volume of the compound, and the contact area between the electrolyte and the electrode, respectively. In this article, the geometric mean (geomean) was adopted to measure the average value of sodium-ion diffusion coefficients during charge or discharge process, which were calculated as

$$\text{Geomean}_{D_{\text{Na}^+}} = \sqrt[n]{D_1 D_2 D_3 D_4 \cdots D_n} \quad (5)$$

Both CV and EIS were applied at a four-channel multifunctional electrochemical workstation (Versa STAT MC, America). The EIS measurements were tested in the frequency range of 0.01 Hz–100 kHz and at the cell voltage of 2.8 V.

Data availability

The data are available within the paper and its Supplementary information file or from the corresponding author upon reasonable request. Source data are provided with this paper.

Received: 31 March 2021; Accepted: 22 July 2021;
Published online: 12 August 2021

References

- Whittingham, M. S. Lithium batteries and cathode materials. *Chem. Rev.* **104**, 4271–4302 (2004).
- Goodenough, J. B. & Kim, Y. Challenges for rechargeable Li batteries. *Chem. Mater.* **22**, 587–603 (2010).
- Vaalma, C., Buchholz, D., Weil, M. & Passerini, S. A cost and resource analysis of sodium-ion batteries. *Nat. Rev. Mater.* **3**, 18013 (2018).
- Yabuuchi, N., Kubota, K., Dahbi, M. & Komaba, S. Research development on sodium-ion batteries. *Chem. Rev.* **114**, 11636–11682 (2014).
- Nayak, P. K., Yang, L., Brehm, W. & Adelhelm, P. From lithium-ion to sodium-ion batteries: advantages, challenges, and surprises. *Angew. Chem., Int. Ed.* **57**, 102–120 (2018).
- Li, X., Zhao, L., Li, P., Zhang, Q. & Wang, M.-S. In-situ electron microscopy observation of electrochemical sodium plating and stripping dynamics on carbon nanofiber current collectors. *Nano Energy* **42**, 122–128 (2017).
- Mizushima, K., Jones, P. C., Wiseman, P. J. & Goodenough, J. B. Li_xCoO₂ (0 < x < 1): a new cathode material for batteries of high energy density. *Mater. Res. Bull.* **15**, 783–789 (1980).
- Myung, S.-T. et al. Nickel-rich layered cathode materials for automotive lithium-ion batteries: achievements and perspectives. *ACS Energy Lett.* **2**, 196–223 (2016).
- Zuo, W. et al. Li-rich cathodes for rechargeable Li-based batteries: reaction mechanisms and advanced characterization techniques. *Energy Environ. Sci.* **13**, 4450–4497 (2020).
- Lu, Z. & Dahn, J. R. In situ X-ray diffraction study of P2-Na_{2/3}Ni_{1/3}Mn_{2/3}O₂. *J. Electrochem. Soc.* **148**, A1225 (2001).
- Zu, C.-X. & Li, H. Thermodynamic analysis on energy densities of batteries. *Energy Environ. Sci.* **4**, 2614 (2011).
- Ammundsen, B. & Paulsen, J. Novel lithium-ion cathode materials based on layered manganese oxides. *Adv. Mater.* **13**, 943–956 (2001).
- Kumakura, S., Tahara, Y., Kubota, K., Chihara, K. & Komaba, S. Sodium and manganese stoichiometry of P2-type Na_{2/3}MnO₂. *Angew. Chem., Int. Ed.* **55**, 12760–12763 (2016).
- Yabuuchi, N. et al. P2-type Na_x[Fe_{1/2}Mn_{1/2}]O₂ made from earth-abundant elements for rechargeable Na batteries. *Nat. Mater.* **11**, 512–517 (2012).
- Yang, L. et al. Lithium-doping stabilized high-performance P2-Na_{0.66}Li_{0.18}Fe_{0.12}Mn_{0.7}O₂ cathode for sodium ion batteries. *J. Am. Chem. Soc.* **141**, 6680–6689 (2019).
- Kwon, M. S. et al. P2 orthorhombic Na_{0.7}[Mn_{1-x}Li_x]O_{2+y} as cathode materials for Na-ion batteries. *ACS Appl. Mater. Interfaces* **9**, 14758–14768 (2017).
- Billaud, J. et al. Na_{0.67}Mn_{1-x}Mg_xO₂ (0 ≤ x ≤ 0.2): a high capacity cathode for sodium-ion batteries. *Energy Environ. Sci.* **7**, 1387–1391 (2014).
- Buchholz, D., Vaalma, C., Chagas, L. G. & Passerini, S. Mg-doping for improved long-term cyclability of layered Na-ion cathode materials—the example of P2-type Na_xMg_{0.11}Mn_{0.89}O₂. *J. Power Sources* **282**, 581–585 (2015).
- Clément, R. J. et al. Structurally stable Mg-doped P2-Na_{2/3}Mn_{1-y}Mg_yO₂ sodium-ion battery cathodes with high rate performance: insights from electrochemical, NMR and diffraction studies. *Energy Environ. Sci.* **9**, 3240–3251 (2016).
- Zuo, W. et al. Highly-stable P2-Na_{0.67}MnO₂ electrode enabled by lattice tailoring and surface engineering. *Energy Storage Mater.* **26**, 503–512 (2020).
- Wu, X. et al. P2-type Na_{0.66}Ni_{0.33-x}Zn_xMn_{0.67}O₂ as new high-voltage cathode materials for sodium-ion batteries. *J. Power Sources* **281**, 18–26 (2015).
- Liu, X. et al. P2-Na_{0.67}Al_xMn_{1-x}O₂: cost-effective, stable and high-rate sodium electrodes by suppressing phase transitions and enhancing Na⁺ mobility. *Angew. Chem., Int. Ed.* **58**, 18086–18095 (2019).
- Han, D. W. et al. Aluminum manganese oxides with mixed crystal structure: high-energy-density cathodes for rechargeable sodium batteries. *ChemSusChem* **7**, 1870–1875 (2014).
- Liu, X. et al. Al and Fe-containing Mn-based layered cathode with controlled vacancies for high-rate sodium ion batteries. *Nano Energy* **76**, 104997 (2020).
- Bordet-Le Guenne, L., Deniard, P., Biensan, P., Siret, C. & Brec, R. Structural study of two layered phases in the Na_xMn_yO₂ system. Electrochemical behavior of their lithium substituted derivatives. *J. Mater. Chem.* **10**, 2201–2206 (2000).
- Zhao, C. et al. Rational design of layered oxide materials for sodium-ion batteries. *Science* **370**, 708–711 (2020).
- Delmas, C., Fouassier, C. & Hagenmuller, P. Structural classification and properties of the layered oxides. *Phys. B+C* **99**, 81–85 (1980).
- Wang, K. et al. Recent advances and historical developments of high voltage lithium cobalt oxide materials for rechargeable Li-ion batteries. *J. Power Sources* **460**, 228062 (2020).
- Zhang, J.-N. et al. Trace doping of multiple elements enables stable battery cycling of LiCoO₂ at 4.6 V. *Nat. Energy* **4**, 594–603 (2019).
- Ohzuku, T. & Ueda, A. Solid-state redox reactions of LiCoO₂ (R3m) for 4 Volt secondary lithium cells. *J. Electrochem. Soc.* **141**, 2972–2977 (2019).
- Li, W., Asl, H. Y., Xie, Q. & Manthiram, A. Collapse of LiNi_{1-x}Co_xMn_yO₂ lattice at deep charge irrespective of nickel content in lithium-ion batteries. *J. Am. Chem. Soc.* **141**, 5097–5101 (2019).
- Lebens-Higgins, Z. W. et al. Revisiting the charge compensation mechanisms in LiNi_{0.8}Co_{0.2-y}Al_yO₂ systems. *Mater. Horiz.* **6**, 2112–2123 (2019).
- Bi, Y. et al. Reversible planar gliding and microcracking in a single-crystalline Ni-rich cathode. *Science* **370**, 1313–1317 (2020).
- Zuo, W. et al. The stability of P2-layered sodium transition metal oxides in ambient atmospheres. *Nat. Commun.* **11**, 3544 (2020).
- Gale, J. F. W., Laubach, S. E., Olson, J. E., Eichhuble, P. & Fall, A. Natural fractures in shale: a review and new observations. *AAPG Bull.* **98**, 2165–2216 (2014).
- Clément, R. J., Bruce, P. G. & Grey, C. P. Review—manganese-based P2-type transition metal oxides as sodium-ion battery cathode materials. *J. Electrochem. Soc.* **162**, A2589–A2604 (2015).
- Conway, B. E., Birss, V. & Wojtowicz, J. The role and utilization of pseudocapacitance for energy storage by supercapacitors. *J. Power Sources* **66**, 1–14 (1997).
- Augustyn, V. et al. High-rate electrochemical energy storage through Li⁺ intercalation pseudocapacitance. *Nat. Mater.* **12**, 518–522 (2013).
- Li, R. et al. Direct growth of Fe₃O₄-MoO₃ hybrid nanofilm anode with enhanced electrochemical performance in neutral aqueous electrolyte. *Prog. Nat. Sci.: Mater. Int.* **26**, 258–263 (2016).
- Zuo, W. et al. Structure-performance relationship of Zn²⁺ substitution in P2-Na_{0.66}Ni_{0.33}Mn_{0.67}O₂ with different Ni/Mn ratios for high-energy sodium-ion batteries. *ACS Appl. Energy Mater.* **2**, 4914–4924 (2019).
- Ohzuku, T., Kitagawa, M. & Hirai, T. Electrochemistry of manganese dioxide in lithium nonaqueous cell: III. X-ray diffractational study on the reduction of spinel-related manganese dioxide. *J. Electrochem. Soc.* **137**, 769–775 (1990).

42. Ohzuku, T., Ueda, A. & Yamamoto, N. Zero-strain insertion material of Li $[\text{Li}_{1/3}\text{Ti}_{5/3}]\text{O}_4$ for rechargeable lithium cells. *J. Electrochem. Soc.* **142**, 1431–1435 (1995).
43. Cho, J., Kim, Y. J., Kim, T.-J. & Park, B. Zero-strain intercalation cathode for rechargeable Li-Ion cell. *Angew. Chem.* **113**, 3471–3473 (2001).
44. Delmas, C., Maccario, M., Croguennec, L., Le Cras, F. & Weill, F. Lithium deintercalation in LiFePO_4 nanoparticles via a domino-cascade model. *Nat. Mater.* **7**, 665–671 (2008).
45. Clément, R. J. et al. Direct evidence for high Na^+ mobility and high voltage structural processes in $\text{P2-Na}_x[\text{Li}_y\text{Ni}_z\text{Mn}_{1-y-z}]\text{O}_2$ ($x, y, z \leq 1$) cathodes from solid-state NMR and DFT calculations. *J. Mater. Chem. A* **5**, 4129–4143 (2017).
46. Kresse, G. & Hafner, J. Ab initio molecular dynamics for liquid metals. *Phys. Rev. B Condens Matter* **47**, 558–561 (1993).
47. Kresse, G. & Furthmüller, J. Efficient iterative schemes for ab initio total-energy calculations using a plane-wave basis set. *Phys. Rev. B* **54**, 11169–11186 (1996).
48. Perdew, J. P., Burke, K. & Ernzerhof, M. Generalized gradient approximation made simple. *Phys. Rev. Lett.* **77**, 3865–3868 (1996).
49. Lee, K., Murray, E. D., Kong, L., Lundqvist, B. I. & Langreth, D. C. Higher-accuracy van der Waals density functional. *Phys. Rev. B* **82**, 081101 (2010).
50. Laurencin, D. et al. Probing the calcium and sodium local environment in bones and teeth using multinuclear solid state NMR and X-ray absorption spectroscopy. *Phys. Chem. Phys.* **12**, 1081–1091 (2010).
51. Yang, T. et al. Introduction of the X-ray diffraction beamline of SSRF. *Nucl. Sci. Technol.* **26**, 020101 (2015).
52. Gao, M. et al. Facile usage of a MYTHEN 1K with a Huber 5021 diffractometer and angular calibration in operando experiments. *J. Appl. Crystallogr.* **49**, 1182–1189 (2016).

Acknowledgements

This work was financially supported by the National Key Research and Development Program of China (grant nos 2018YFB0905400, 2016YFB0901502), National Natural Science Foundation of China (grant nos 21761132030, 21935009, U1932201), the Fundamental Research Funds for the Central Universities (grant no. 20720200075), and the “Double-First Class” Foundation of Materials and Intelligent Manufacturing Discipline of Xiamen University. The authors thank Dr. Dong Su for the kind help and insightful discussions. W.Z. acknowledges the research fellowship from the Alexander von Humboldt Foundation. G.F.O. acknowledges the financial support from Spanish ministry of science and innovation (project n° MAT2017-84002-C2-1-R). R.F. acknowledges the support from the National High Magnetic Field Laboratory which is supported by NSF Cooperative Agreement DMR-1644779 and the State of Florida. The authors gratefully acknowledge the valuable beamtime from beamline BL14B1 of the SSRF.

Author contributions

W.Z., M.-S.W., and Y.Y. conceived the project. Y.Y. supervised the project. W.Z., J.Q., X.L., Y.L., M.-S.W., and Y.Y. designed the experiments. W.Z. and J.Q. performed the materials synthesis and electrochemical testing. W.Z., J.Q., X.L., Z.X., J.X., J.W., G.F.O., W.W., and Y.L. performed the characterizations. D.Z. and S.W. completed the computational calculations. W.Z., J.Q., X.L., F.R., D.Z., Z.X., Y.L., S.W., R.F., M.-S.W., and Y.Y. analyzed the data and proposed the mechanisms. W.Z. and Y.Y. wrote the initial paper. All authors discussed the results and commented on the manuscript.

Competing interests

The authors declare no competing interests.

Additional information

Supplementary information The online version contains supplementary material available at <https://doi.org/10.1038/s41467-021-25074-9>.

Correspondence and requests for materials should be addressed to M.-S.W. or Y.Y.

Peer review information *Nature Communications* thanks Surendra Martha and the other, anonymous, reviewer(s) for their contribution to the peer review of this work.

Reprints and permission information is available at <http://www.nature.com/reprints>

Publisher's note Springer Nature remains neutral with regard to jurisdictional claims in published maps and institutional affiliations.



Open Access This article is licensed under a Creative Commons Attribution 4.0 International License, which permits use, sharing, adaptation, distribution and reproduction in any medium or format, as long as you give appropriate credit to the original author(s) and the source, provide a link to the Creative Commons license, and indicate if changes were made. The images or other third party material in this article are included in the article's Creative Commons license, unless indicated otherwise in a credit line to the material. If material is not included in the article's Creative Commons license and your intended use is not permitted by statutory regulation or exceeds the permitted use, you will need to obtain permission directly from the copyright holder. To view a copy of this license, visit <http://creativecommons.org/licenses/by/4.0/>.

© The Author(s) 2021